

# Flow Casting Soft Shells with Geometrical Complexity and Multifunctionality

Dongliang Fan, Yuxuan Liao, Wenyu Wu, Ping Zhang, Xin Yang, Renjie Zhu, Yifei Wang, Canhui Yang, and Hongqiang Wang\*

Soft shells are ubiquitous in soft devices, e.g., soft robots, wearable sensors, and soft medial replicas. However, previous widely accepted methods, such as mold casting, dip coating, and additive manufacturing, are limited to thick shells due to the mold assembly and the large friction during demolding, long processing time for mold dissolution, and poor scalability, respectively. Here, a facile, robust, and scalable manufacturing technique, named flow casting, to create soft shells with complex geometries and multifunctionalities is proposed. The method involves a flow-governed layer casting process and a peel-dominated demolding process. A one-dimensional soft shell is first made with controllable thicknesses (100–400  $\mu\text{m}$ ) and fabricated various soft shells of intricate geometries, including three-branched, circular-shaped, and exquisite microstructures such as papillae and microgrooves on curved surfaces, with the resolution of feature sizes on the order of 100  $\mu\text{m}$ . Furthermore, the versatility of this method is demonstrated with a 3D vascular phantom model for a magnetic robot transporting, microstructured cubic sleeves for enhancing the grasping ability of rigid grippers, and a stretchable optical waveguide capable of color changing by external mechanical stimuli.

generate more complex reactions,<sup>[5,6,9–11]</sup> and the soft sensors achieve high agility and robustness with the three-dimensional (3D) complex geometries of the shells.<sup>[12–15]</sup> Monolithic thin, soft shells exhibited their importance in medical devices, such as 3D vascular replicas, for training trainee surgeons before clinical operations.<sup>[16]</sup> Soft shells with microstructure on the outer surfaces display a friction enhancement.<sup>[17,18]</sup> Therefore, appropriate fabrication technologies for soft bodies containing hollow structures and complex geometry are crucial for the soft devices' functionality.

Yet, existing soft shell fabrication technologies suffer from limited geometry, long processing time, and poor scalability. For example, mold casting is a general fabrication method for soft shell devices,<sup>[19,20]</sup> but the fabricated shells are limited to millimeter-scale due to the large friction between the soft shell and the molds.<sup>[19]</sup>

Also, the molds, composed of a central core mold and two outer halves, greatly restrict the 3D design flexibility. The dip-coating method has been employed for both 1D hollow soft robotics and 3D hollow vascular replicas fabrication,<sup>[6,16,21]</sup> but the mold dissolution process is time-consuming and may cause buckling in soft shells.<sup>[22]</sup> Whereas additive manufacturing could directly print 3D soft shells with high topological complexity for soft robotics,<sup>[4,23,24]</sup> it is hard to generate a smooth surface due to the

## 1. Introduction

Soft materials are extensively adopted in soft microfluidics<sup>[1,2]</sup> and soft robotics,<sup>[3–6]</sup> which have benefited and thrived in broad research in recent decades due to their high compliance and stretchability.<sup>[7,8]</sup> Studies in soft devices drastically increase in the last decades in various fields, particularly in human–machine interactions. For instance, the soft robots

D. Fan, Y. Liao, X. Yang, R. Zhu, H. Wang  
Shenzhen Key Laboratory of Biomimetic Robotics  
and Intelligent Systems  
Department of Mechanical and Energy Engineering  
Southern University of Science and Technology  
Shenzhen, Guangdong 518055, China  
E-mail: wanghq6@sustech.edu.cn

D. Fan, Y. Liao, X. Yang, R. Zhu, H. Wang  
Guangdong Provincial Key Laboratory of Human-Augmentation  
and Rehabilitation Robotics in Universities  
Department of Mechanical and Energy Engineering  
Southern University of Science and Technology  
Shenzhen, Guangdong 518055, China

W. Wu  
School of System Design and Intelligent Manufacturing  
Southern University of Science and Technology  
Shenzhen, Guangdong 518055, China

P. Zhang, Y. Wang, C. Yang  
Shenzhen Key Laboratory of Soft Mechanics & Smart Manufacturing  
Department of Mechanics and Aerospace Engineering  
Southern University of Science and Technology  
Shenzhen, Guangdong 518055, China

H. Wang  
Southern Marine Science and Engineering Guangdong Laboratory  
(Guangzhou)  
Guangzhou 510000, China

 The ORCID identification number(s) for the author(s) of this article can be found under <https://doi.org/10.1002/admt.202201640>.

DOI: 10.1002/admt.202201640

layer-by-layer printing process and not a general approach for the scalability and mass production of soft hollow structures. Recently, bubble casting was developed to generate soft shells by blowing the liquid precursor through molds, which exhibit excellent design flexibility and fabrication scalability,<sup>[5]</sup> but only the planar geometries were presented.

Here, we proposed a simple, fast, one-mold-required, and versatile method, named flow casting, to fabricate monolithic soft complex 3D hollow structures. Compared with other manufacturing technologies for thin layers<sup>[5,16,19,21]</sup> (Table S1, Supporting Information), flow casting shares similar fluidics mechanisms—elastomer precursors flow through the inner wall of the mold and remain a thin, soft layer. However, the proposed method, flow casting, is advantageous in two aspects: great design flexibility for 3D complex soft shells and a fast and one-mold-required demolding process. Compared with mold casting for simple geometries,<sup>[19]</sup> the design flexibility of flow casting is satisfied by various mold manufacturing methods, e.g., 3D printing. Additionally, unlike additive manufacturing for soft shells,<sup>[23]</sup> whose surface properties highly depend on printing accuracy, both smooth and microstructured outer surfaces can be generated by exactly duplicating the fine feature of the molds' inner wall, according to

the flow-governed layer casting process. Moreover, different from other casting technologies requiring multiple mold assembly,<sup>[5,19]</sup> only one mold is needed in flow casting. The peel-dominated demolding mechanism, resulting from the mechanical difference between the soft layer and the rigid mold, presents its superiority in the gentle, fast, solvent-free demolding process over dip coating and other casting methods, whose demolding processes suffer from long processing time for mold dissolution,<sup>[16]</sup> and strenuous process for multiple molds separation.<sup>[5,19]</sup>

In this work, we built theoretical models for the layer thickness distribution and thickness control during the layer casting process and introduced and analyzed the peel-dominated demolding process to rationalize this flow casting technology to produce complex 3D thin, soft, hollow structures with smooth or microstructured surfaces. We validated this technology for complex structure fabrication by producing a series of 3D soft shells with inner connections, soft tubular structures with topologic complexity, and microstructure. Finally, we demonstrated this flow casting technology with a 3D soft vascular replica, soft, microstructured, thin cubic sleeves for rigid grippers, and a three-branched soft optical waveguide for color changing (Figure 1A).

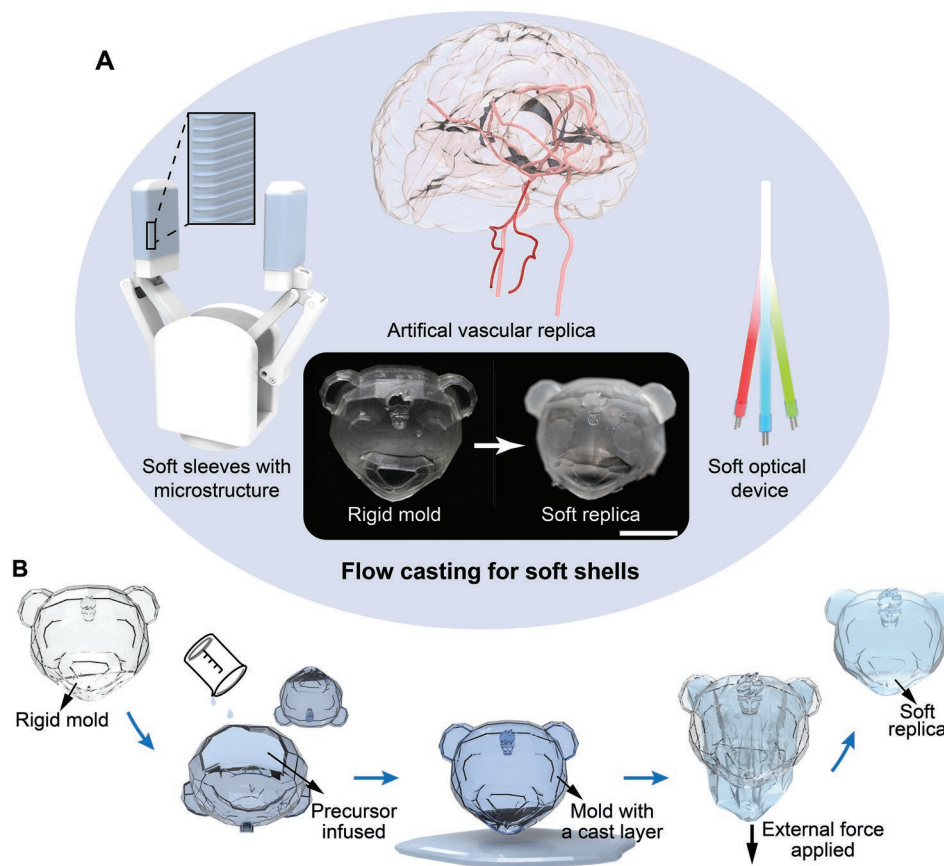


**Figure 1.** Applications and fabrication process of flow-cast soft, thin shells. A) Schematic demonstrating the diverse applications of flow casting, including artificial vascular replica, microstructured soft sleeves for rigid robots, and soft optical devices. The bottom figure shows the digital images of a printed panda mold and the flow-cast soft shell replica (Ecoflex 0050, curing at 60 °C for 8 h). Scale bar, 10 mm. B) Schematic of the fabrication process. The precursor of a soft shell is poured into a mold of a panda shape. Then, the precursor is drained out, leaving a thin layer on the inside wall of the mold. After curing, the soft shell is demolded facilely via peeling, without damaging the mold, to obtain a soft replica.

## 2. Results and Discussion

### 2.1. Soft Shells with Predictable Thickness in Flow Casting

A typical flow casting for soft shells is exhibited in Figure 1B and Movie S1 (Supporting Information). Given a rigid hollow mold (e.g., in a panda head shape), the elastomer precursor was poured into the mold and drained out from the flipped mold, leaving a thin layer of precursor on the mold's inner surface due to surface tension and viscosity. After thermally cured into elastomer, the soft shell was delaminated from the mold by peeling. The rigid panda model and the soft-shell replica generated are shown in Figure 1A. During the fabrication process, the interaction between the casting fluid and the target surface is also essential to flow casting. Before the precursor cures, the contact angle between the casting fluid and the target surface should be smaller than 90° to form a liquid layer in the mold surface (Figure S1, Supporting Information). After the precursor cures, the chemical reaction should not occur between the precursor and the target surface in case of building a strong adhesion between them, which may hinder the later demolding process. In our casting system, only weak adhesion is built at the interface; therefore, no cured elastomer will remain in the mold (Figure S2, Supporting Information). In addition, the contaminant on the surface may prevent the curing process of the casting fluid, and the uncured elastomer will contaminate the surface and limit mold reusability. Therefore, the mold surface should be carefully cleaned.

In flow casting, controlling the shell's thickness is challenging due to the time-dependent viscosity of precursors and gravity. We quantitatively investigated the variation of shell thickness using a 1D soft tube. A series of experiments were conducted by flow casting silicone precursor (Ecoflex 0050, Smooth-On) on acrylic tubes (inner diameter: 4 mm) to analyze the thickness distribution. The fabrication process is schematized in Figure 2A. An acrylic tube (inner diameter: 4 mm) is first prepared, and its bottom end is fixed by a printed pedestal and sealed by a plugging block. Then, the tube is filled with silicone precursor. After being drained out, a thin layer of a precursor is left on the inside wall of the tube and cured thermally. The soft-shell thickness can be tuned by the viscosity of the precursor, which could be adjusted by the waiting time before the precursor flows out of the mold (see Figure 2B; Figure S3, Supporting Information). As the waiting time increases, the precursor viscosity increases due to the cross-link reaction,<sup>[25]</sup> which results in a thicker cast layer on the mold. The layer thickness  $h$  is governed by:

$$h(z,t) = \sqrt{\frac{z}{\frac{\rho g}{\beta \mu_0}(\beta t - \ln \mu) + C}} \quad (1)$$

where  $z$  is the position,  $t$  is the waiting time,  $\rho$  is the density,  $g$  is the acceleration of gravity,  $\beta$  is the prefactor,  $\mu_0$  is the initial viscosity,  $\mu$  is the viscosity at time  $t$ , and  $C$  is a constant (layer thickness control, Supporting Information). As shown in Figure 2B, the thickness increases with the waiting time increasing, and the analytical and numerical predictions

agree well with the experimental data. The thickness of produced tubes ranges from 100 to 400  $\mu\text{m}$  for slip casting once, and a broader range is available when multiple castings are applied. We also analyzed the thickness profile of the tube and found that the soft layer thickness increases along the top-to-bottom direction (from 150 to 300  $\mu\text{m}$ ) due to the influence of gravity, and both analytical and numerical results fit well with the experimental data, as shown in Figure 2C. Thus, we coated the shell with flow casting twice by flipping the mold's bottom up the second time and finally achieved a uniform thickness along with the whole tubular structure, as shown in Figure 2D. Moreover, the surface roughness of these soft tubes  $S_a$  is tens of nanometers, which is smoother than those produced by 3D printing ( $S_a$  is more than 0.99  $\mu\text{m}$ <sup>[26]</sup>), as shown in Figure S4 (Supporting Information) and Experimental Section.

The demolding process is another trait of flow casting. Compared with multiple mold assembly for other casting technologies,<sup>[5,19]</sup> flow casting only requires one mold and avoids the tedious assembly process. Furthermore, the Poisson effect and the hollow structure of highly stretchable soft materials greatly facilitate the shell delamination process by shrinking the cross-sectional area of soft shells when an external force is applied. Additionally, the large difference in stretchability mismatch between the rigid mold and the soft shell would guarantee the integrity of the soft shell when breaking the mold is necessary (just like breaking a boiled egg's shell).

Experiments were conducted to characterize the demolding process of soft shells (see Movie S2, Supporting Information). Samples for the demolding process were prepared by the flow casting process (see Figure 2A). Due to the high stretchability of the elastomer, the soft shell vastly reduced its cross-sectional area to initiate the peel-dominated demolding process when an external force was applied (Figure 2E; Figure S5, Supporting Information). On the other hand, excessive soft shells underwent a much longer strain, which may reach the strain limit of the soft shells before the demolding was finished. We chose two different elastic materials, Ecoflex 0050 and a mixture (mass ratio of Ecoflex 0030: Dragon skin 30 = 1:2), for demolding tests. The mixture showed a larger Young's modulus and a smaller rupture strain compared with Ecoflex 0050 (Figure S5, Supporting Information). Moreover, the higher modulus soft shells result in a quicker and more fluent demolding process (characteristics of the demolding process, Supporting Information). Different from the regular demolding or peel processes, soft shell demolding exhibits a discrete peel process, as shown in Figure 2F. This phenomenon perhaps resulted from the assembly error, and the applied force deviated from the center of the acrylic tube, making the deformation of the soft shell asymmetric. The side of the soft shell with a larger peel angle first initiated the demolding process. Along with the crack propagation, the other side generated a larger angle to activate the demolding. Then, the demolding process repeated this cycle till the demolding was finished. To verify the effect of assembly deviation, we apply a 2-mm deviation of the applied force to this experiment system, and an obvious discrete peeling in the elastic shell demolding process was demonstrated (Figures S5 and S6, Supporting Information).

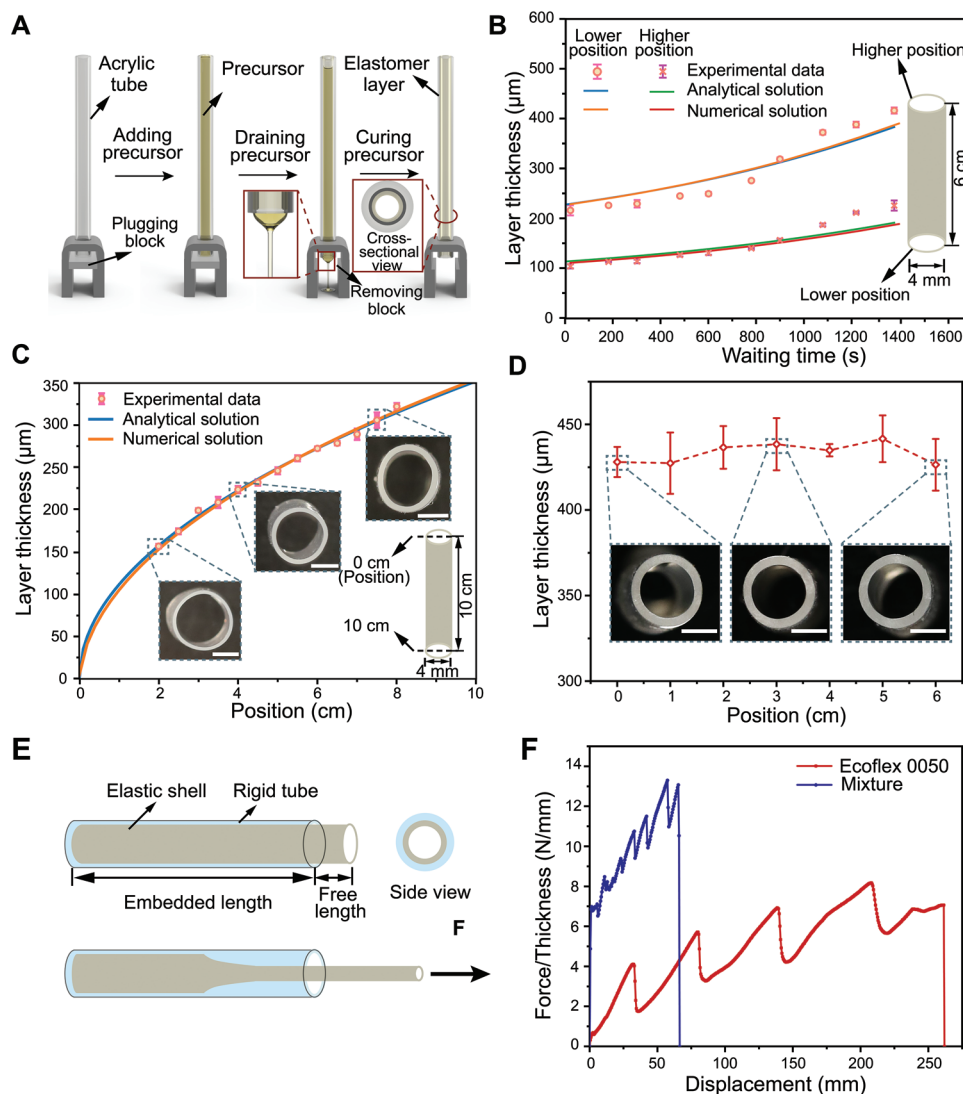


**Figure 2.** Fabrication and characterizations of soft tubes. A) Schematic of the fabrication process. B) The effect of waiting time on layer thickness. C) The relationship between position and layer thickness. D) The layer thickness distribution for twice flow casting (the mold was inverted, and the second flow casting was conducted). Scale bars, 2 mm. E) Structure of samples for demolding test and the schematic plot during the demolding process. F) Force-displacement curves of the demolding process for Ecoflex 0050 and the mixture. The data in (B–D) are presented as mean values  $\pm$  standard deviation with the sample size  $n = 3$ .

## 2.2. Complex Soft Shells via Flow Casting

According to the flow casting of soft materials, a collection of novel hollow structures with geometrical complexity and microstructures are demonstrated in **Figure 3**. The geometry of a straight soft tube connected with three branches, a circular tube, and its derivative structures, a spherical branch soft tube, and a “ $\Phi$ ”-shaped branch soft tube (Figure 3A–D) were produced. The soft-shell structures with equally distributed topological geometries, consisting of protruding circular edges, corrugated geometries, and segmented gear structures, are shown in Figure 3E–G. In addition, microstructures, i.e., papillae and microgrooves with fine features of 100  $\mu\text{m}$ , were embossed on the outer surface of the soft tube (outer diameter: 2 mm, length: 50 mm), as shown in Figure 3H–K. The

resolution of microstructures is determined by the precision of the mold and the surface energy and shear modulus of the elastomer. Following a similar fabrication process, casting elastomer precursors onto target surfaces to fill the microstructures, as soft lithography, whose minimum accessible feature size is around 50–100 nm,<sup>[27]</sup> the inner surface geometry information of the mold can be exactly copied by the flow casting method. Compared with slip casting, soft shells fabricated by dip coating and bubble casting tended to possess a smooth surface due to their applications in soft vascular replicas<sup>[6]</sup> and soft robotics.<sup>[5,21]</sup> The complex array feature with a resolution of 400  $\mu\text{m}$  for soft robotics was fabricated by mold casting.<sup>[20]</sup> For 3D printing soft shells, the resolution of the feature sizes is around 150–350  $\mu\text{m}$  for the printed pneumatic robots on the planar surface.<sup>[24]</sup> Therefore, flow casting seems a promising



**Figure 3.** Soft shells with complex geometries and elaborate structures. A–D) Soft shells with inner connection structures, including a three-branched tube, a spherical-branched tube, a “Φ”-shaped branch tube, and a circular-shaped tube. Scale bar, 1 cm. E–G) Soft shells with uniformly distributed topological geometries, including circular edges, corrugated geometries, and segmented gear structures. Scale bar, 1 cm. H–K) Soft shells with microstructures. H) Shows a shell with microstructures of papillae, and J) Zooms in the microstructures. I) Shows a shell with microgrooves, and K) Zooms in the microstructures. The scale bars are 2 mm in (H, I) and 1 mm in (J, K). L) Fabrication process of the soft replica of a human hand. M) The front and side views of the soft shell of a human hand replica. Scale bars, 2 cm. N) The feature parts of the replica. Scale bars, 5 mm.

technology to generate large-area microstructures on soft curved shells.

Currently, bionic prosthetic hands can achieve general tasks, such as grasping and lifting, just like real human hands.<sup>[28,29]</sup> These prosthetic hands are always made of rigid components, which may not be safe when interacting with environments. Moreover, some biological information, i.e., fingerprints, is not convenient to emboss onto the rigid prosthetic hands. Therefore, a soft glove with fine features of human hands may offer an approach to overcoming this dilemma. Herein, we generated a soft shell of a human-hand replica via flow casting. The mold of the hand replica was fabricated by immersing the hand in the plaster slurry to accurately replicate the hand’s textures. Then, the soft replica was fabricated by flow casting (Figure 3L). The soft shell of the human-hand replica, shown in Figure 3M,N,

exhibits great potential for bionic prosthetic hands since both the geometry and delicate features of the human hand are precisely copied.

### 2.3. Demonstration of 3D Soft Vascular Replicas

Compared with traditional open surgery, minimally invasive surgery is the predominant operation choice due to the small cut and fast recovery, especially for cardiovascular and cerebrovascular diseases.<sup>[30]</sup> The guidewires have always been used to insert deep into the vessels till reaching the sick plot and exert certain operations. However, the tortuous vessels make it an exquisite-skilled and rich-experienced operation process. Therefore, 3D vascular replicas, which could build preoperative

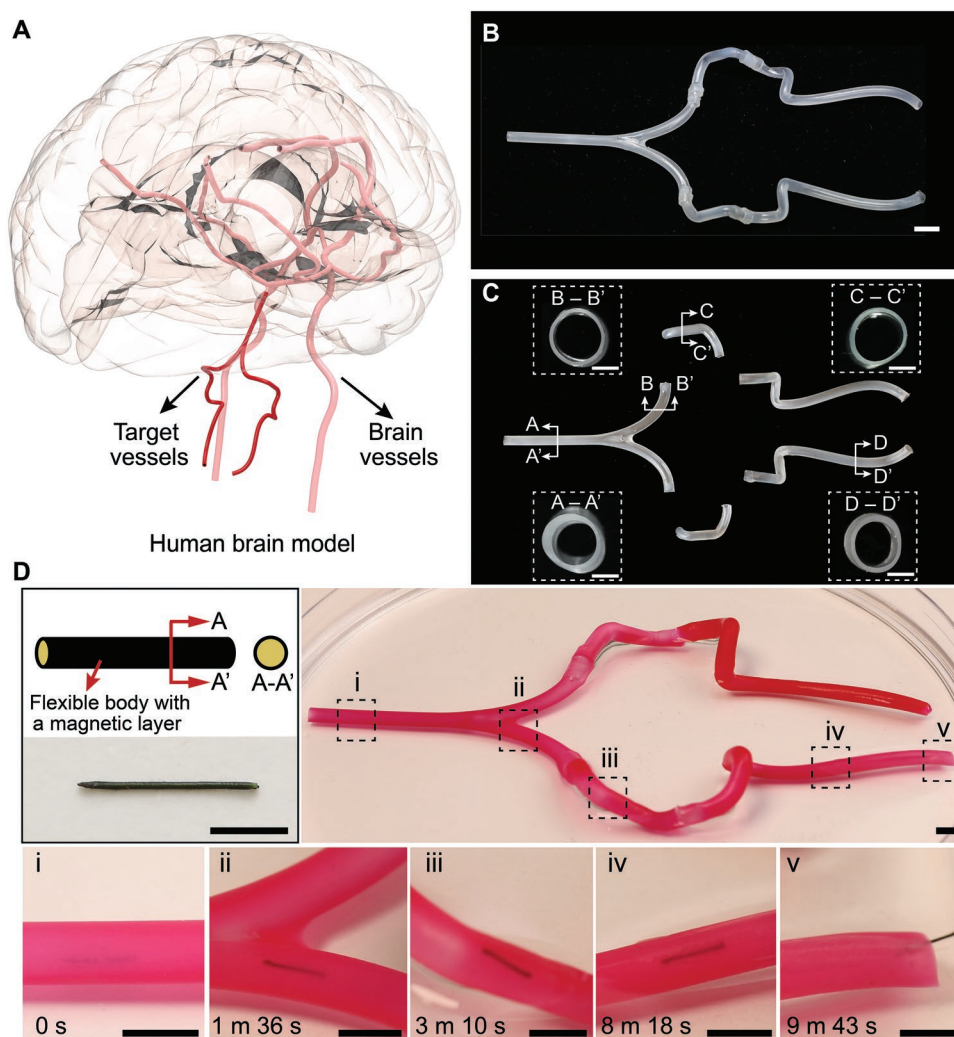


**Figure 4.** 3D soft vascular replica for a magnetic robot. A) Schematic of a human brain model. The red tubes schematize brain vessels, and the dark red ones are the target vessels to be replicated. B) The fabricated 3D soft vascular replica. Scale bar, 10 mm. C) Segmental components of the replica and their cross-sections. Scale bars, 2 mm. D) Demonstration of a small-scale magnetic robot navigating through the red artificial vascular model. The bottom five figures exhibiting the positions of the robot in the vascular model. Scale bars, 5 mm.

simulations, are indispensable training platforms for beginners.<sup>[16,21]</sup> Still, commercial vascular replica fabrication is a labor-intensive and high-cost process. Dip coating for vascular replica fabrication still has various limitations, including nonrecyclability of the mold, swelling of silicone-coating materials, e.g., polydimethylsiloxane (PDMS), and long-time consumption.<sup>[31]</sup>

Flow casting shows its advantages in 3D soft-shell fabrication, mold recyclable, and no solvent required. Here, we generated the segments and the assembled 3D soft brain vascular replica (Figure 4A–C). We chose the more rigid mixture (mass ratio of Ecoflex 0030: Dragon skin 30 = 1:2) for vascular replica flow casting to support its tortuous structure. The Ecoflex 0030 here plays a role in thinning the Dragon skin precursor to make the precursor leak out quickly and softening the Dragon skin elastomer to facilitate the delamination from the substrate facilely. The flow casting process was conducted twice to reach the desired thickness in case the soft shell was torn during delamination. The shell thickness was controlled at 200–400  $\mu\text{m}$  for all

segments. The outer diameter of all the segments was 4 mm, which were connected by rigid tubes to form the whole replica. The produced soft 3D vascular replica exhibited the advantages of flow casting for complex soft-shell fabrication, according to the solvent-free and efficient delamination process. Moreover, we demonstrated the functionality of the artificial vascular replica by coating a lubricating layer (fluorogel) on the inner surface and then manually navigated a small-scale soft magnetic robot through it via a permanent magnet (see Figure 4D; Movie S3, Supporting Information) to exhibit the potential medical applications for cerebrovascular disease treatments.

#### 2.4. Demonstration of the Microstructured Soft Sleeves for Gripping Performance Promotion

Rigid grippers have been extensively employed in manufacturing, package sorting, and our daily life.<sup>[32]</sup> However, their

rigid components limit the grippers for holding heavy items with smooth surfaces or fragile items, and still exist potential safety issues for human–machine interaction.<sup>[33]</sup> Soft grippers exhibit distinctive traits, such as easy control, safe interaction, and fragile object operation due to the high compliance of soft materials recently.<sup>[33]</sup> However, limitations, such as difficulty in modeling and the weak force, still exist in soft grippers due to the high nonlinearity of soft materials. Here, we combine soft layers with rigid grippers to simultaneously embrace high output, precise control, and safe interaction to solve this dilemma. The soft layers not only buffer the interacting force but also enhance the friction force for gripping without impeding the rigid grippers' operations. However, building a strong and reversible bonding between soft materials and rigid substrates, i.e., plastics and metals, is still challenging.<sup>[34]</sup> Herein, fastening soft, thin sleeves (smaller than grippers in dimension) onto rigid grippers is proposed as an alternative. Moreover, inspired by the structure of geckos' feet,<sup>[35]</sup> microstructures embossed onto soft layers could enhance the grasping capacity by increasing the friction force.

Here, we fabricated soft sleeves in cubic geometry (thickness: 200  $\mu\text{m}$ ) containing two microstructures, papillary and wedge-shaped asperities, as shown in **Figure 5A,B**, and insets. Foam layers, which are usually attached to rigid grippers to buffer and increase friction commercially, are used for comparison. Compared with the foam structure, the soft sleeves were worn to a rigid gripper (**Figure 5C**), and friction force tests were conducted under different loads (normal forces), as shown in **Figure S7** (Supporting Information) and Experimental Section. The wedge-shaped structure presents twice the friction force as that of the foam when the load is less than 5.7 N (see **Figure 5D**), attributed to its one-way friction structure. The wedge structures are compressed and gradually become flat as the load increases, so the friction force tends to plateau. We validated the soft sleeves' safe interaction and friction force enhancement by grasping different objects, as shown in **Figure 5E**. Without the soft sleeves, the rigid gripper failed to hold a 200 g weight with a smooth surface and a gel ball with a slippery surface. On the contrary, the rigid gripper with soft sleeves succeeds in holding the 200 g weight, the gel ball, and other items, including a cherry tomato, a screw, a test tube, and a flesh driver (see **Figure 5E**; **Movie S4**, Supporting Information). The replaceable wearable soft sleeves enhance the friction force and effectively extend the grasping ability of rigid grippers.

## 2.5. Demonstration of Soft Optical Waveguides for Color Changing

Optical waveguides are widely used in cytometers,<sup>[36]</sup> sensing dissolved organics and gases,<sup>[37]</sup> and mechanical deformation sensing<sup>[38]</sup> due to their advantages in the small dimension, signal integration, and immunity to external electromagnetic interference (EMI) compared with capacitive and resistive sensors. The optical waveguide is composed of a core–shell structure and reflective index difference.<sup>[39]</sup> Recently, soft sensors embracing complex distributed functional probes were designed for different deformation modes recognition and position detection.<sup>[12,40]</sup> To fabricate a waveguide on a

macroscopic scale, mold casting is a general method to produce 1D soft waveguides for motion detection.<sup>[38,41]</sup> Still, these waveguides' simple geometry and thick shells may hinder their sensitivity.

Here, a flow-cast soft tube (outer diameter: 2 mm, reflective index: 1.41) infused with a biocompatible liquid, glycerol (reflective index: 1.47), a light-emitting diode (LED), and a photodiode constitute a soft optical waveguide, as shown in **Figure 6A**. This soft liquid-core optical waveguide possesses a smooth and round cross-section for homogeneous transmission in any direction and the ultrasoft structure for great adaptability in uneven environments.<sup>[39]</sup> A second flow casting with the tube mold upside down was conducted to achieve a uniform layer thickness (300  $\mu\text{m}$ ). When the soft optical waveguide was subjected to a strain, a linear increase was shown in **Figure 6B** and **Figure S8** (Supporting Information), which is governed by<sup>[41]</sup>:

$$a = 10\epsilon c L_0 \epsilon \quad (2)$$

where  $a$  is the power loss,  $\epsilon$  is the absorptivity,  $c$  is the concentration for chemical species, which is considered a constant,  $L_0$  is the original length, and  $\epsilon$  is the strain.  $10\epsilon c L_0$  is a constant (see details in Experimental Section).

Creatures in nature provide numerous solutions to color changing for camouflage or display.<sup>[42]</sup> Commercially available LEDs offer us an applicable and straightforward approach to achieving color changing. Red, green, and blue are the primary colors for an additive color model to generate a broad color gamut, and the RGB-LED array has also been widely used for liquid crystal displays.<sup>[43]</sup> We designed and fabricated a soft mechanical color adjuster composed of a soft shell in a three-branched geometry, glycerol for light guiding, and three LEDs (red, green, and blue) based on this additive color model, as shown in **Figure 6C** and **Figure S8** (Supporting Information). White light was generated according to the 3D-branched waveguide and the light intensity of the LEDs. When a strain was applied to one of the branches, the intensity loss increased linearly. Therefore, the intensity decreases in any three branches, causing the coloration shift in the color space (**Figure 6D**; **Movie S5**, Supporting Information). In principle, any chromaticity point in the color space can be reached via a combinational deformation of three branches. Moreover, the coloration also reflected the sensory feedback for the deformation of each branch precisely, according to Equation (2). Herein, our soft optical color adjuster combines the external or internal stimuli with our visions by dynamic coloration, which may lead to a new approach to interacting with humans and environments.

## 3. Conclusion

This article proposed a fabrication methodology, flow casting, to produce soft shells with highly complex geometry for versatile soft devices. The straightforward and convenient fabrication processes for both the shell formation and demolding process offer a novel approach to enriching the development of soft devices. We performed a series of experiments for 1D soft tube fabrication to quantitatively understand the layer thickness distribution and its control parameters. We analyzed and built a

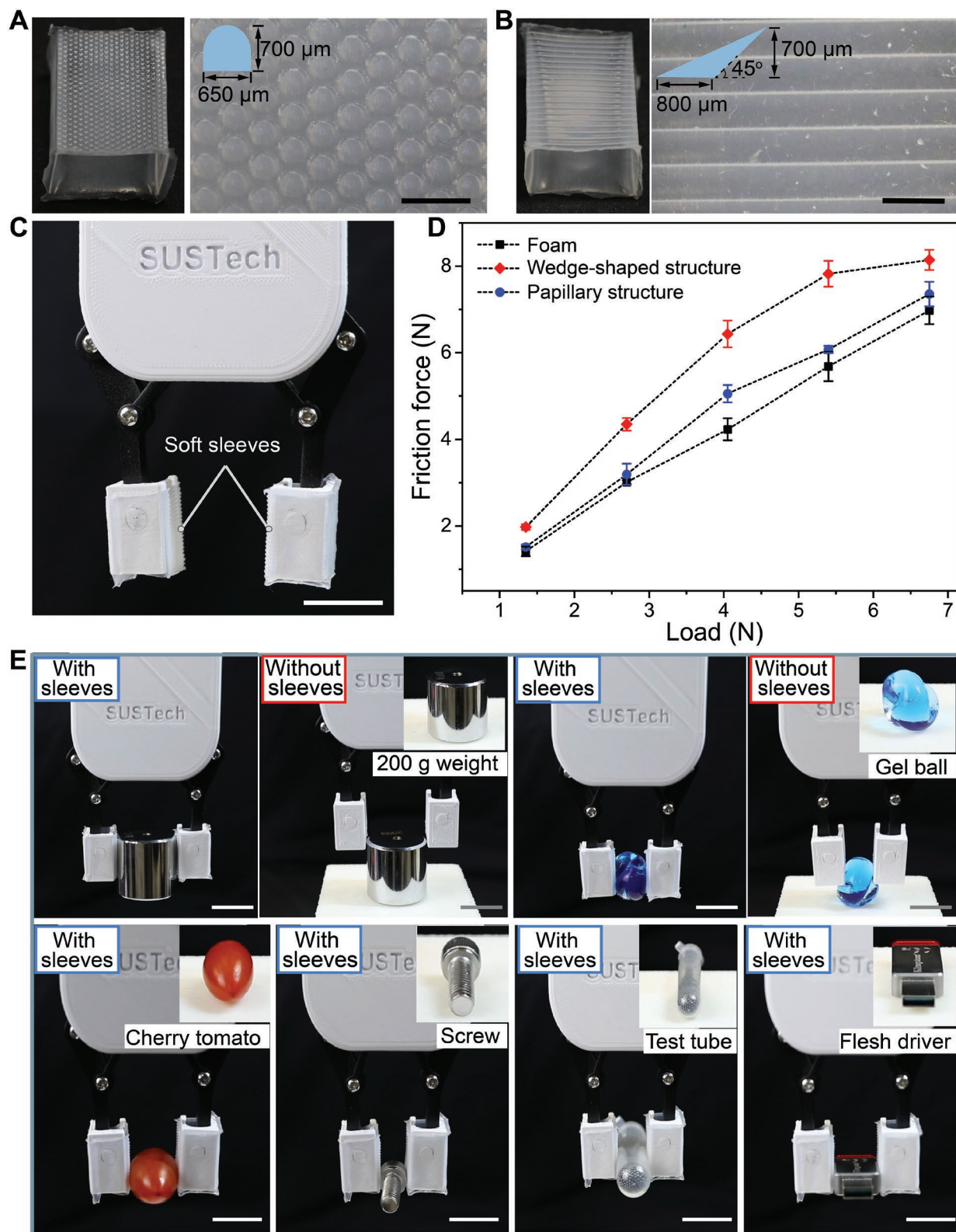


**Figure 5.** Microstructured soft sleeves for rigid grippers. A) Soft-shell structure with papillary asperities. Scale bars, 1 mm. B) Soft-shell structure with long wedge-shaped asperities. Scale bars, 1 mm. C) The soft-shell structures working as soft gloves worn on two rigid grippers. Scale bar, 2 cm. D) Friction force as a function of load for the grippers with different structures. The data are presented as mean values  $\pm$  standard deviation with the sample size,  $n = 3$ . E) Grasping ability of the rigid gripper with or without the soft sleeves. Without the soft sleeves, the gripper failed to hold the 200 g weight with a smooth surface and a gel ball with a slippery surface. The gripper with soft sleeves held a cherry tomato, a screw, a test tube, and a flesh driver to exhibit the grasping ability. Scale bars, 2 cm.

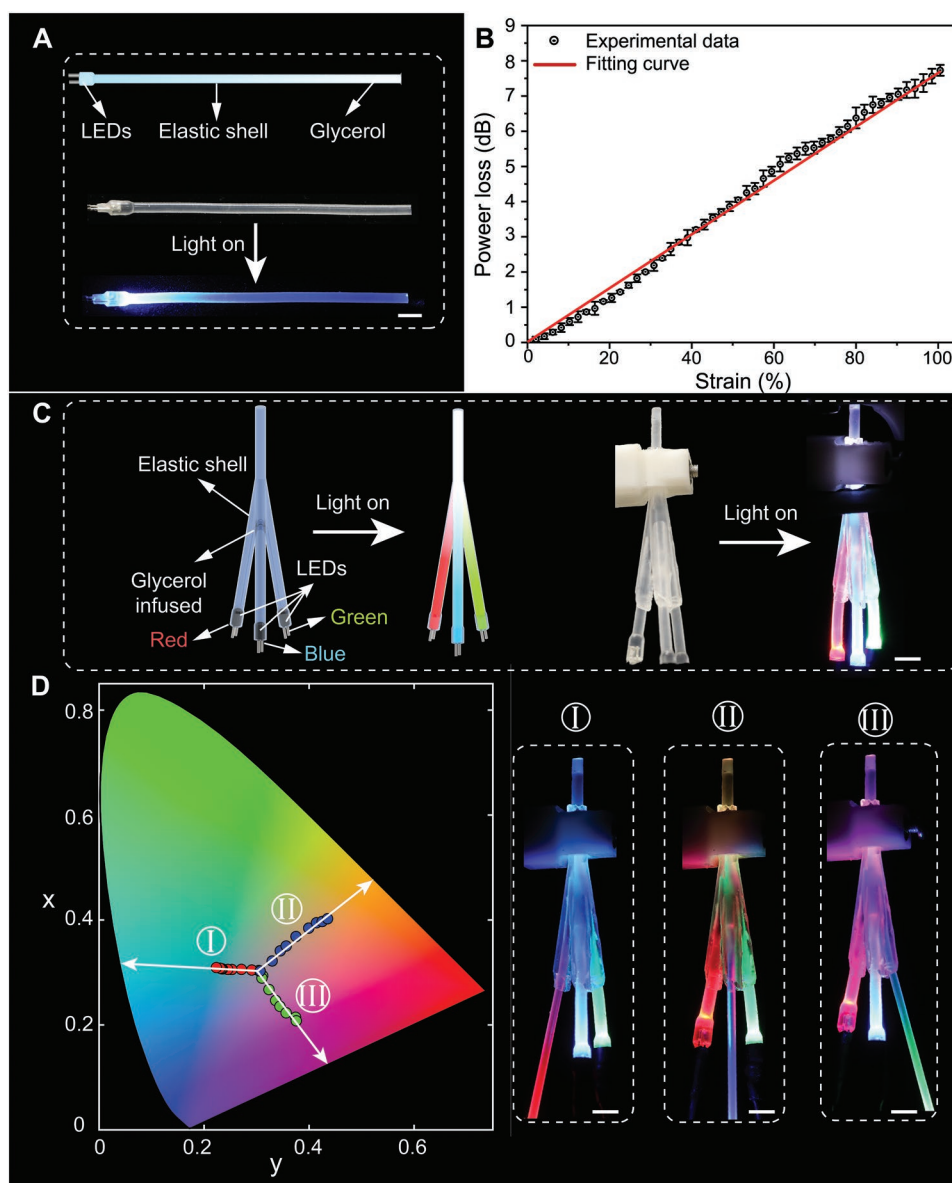


**Figure 6.** Soft shells for soft optical waveguides. A) The schematic and components of a single soft optical waveguide. The soft tube is 13 cm in length and 2 mm in diameter. B) The linear relationship between strain and power loss for a soft optical waveguide. The data are presented as mean values  $\pm$  standard deviation with the sample size,  $n = 3$ . C) Schematic (left) and a digital image showing a strain-dependent soft color adjuster at light-off and light-on states. D) Chromaticity responses with applied strain on different branches. Scale bars, 5 mm.

model for the thickness distribution and the effect of waiting time on thickness. Furthermore, instead of separating the two-part mold for existing casting methods, i.e., molding casting, during demolding, the high stretchability, and Poisson's effect of elastomer endow the soft shell with a peel-dominated demolding process via vastly reducing their cross-sectional area. We also validated that elastomer with a higher modulus is more applicable for the demolding process.

Numerous complex structures, such as soft shells with inner connections, soft shells with equally distributed topological geometries, and soft shells with microstructures, are demonstrated to exhibit the fabrication ability of soft shells. The soft shell of the human-hand replica shows the reproductive

capacity of flow casting for both geometries (on a macroscopic scale) and the texture (on a microscopic scale). The soft 3D vascular replica composed of segments in centimeters presents replaceability and customization for different situations. The cubic soft sleeves were generated for a rigid gripper to increase compliance when interacting with fragile objects, and different microstructures were embossed on the soft shells to enhance their grasping capacity. Finally, we demonstrated a 3D-branched soft optical color adjuster based on external mechanical stimuli. Moreover, the dynamic coloration can be reached via a single or combinational deformation of these three branches.

There are several aspects to improve for flow casting for soft shells. In the theoretical part, we analyzed a simple situation,

a straight tube, for layer thickness distribution. However, in a real situation, complex geometry will inevitably be encountered. Therefore, the effect of curvature on layer thickness should be investigated. Moreover, when the diameter decreases to mesoscale or microscale, the capillary may play a dominant role in layer formation. The demolding process will be more complicated when a curved surface is encountered. Considering these specific situations, a more comprehensive and solid model should be built. In addition, postprocessing, such as rotation along with the axial direction, may improve the homogeneous quality of layers since the precursor prefers to converge at the concave inner surface. The 3D-printed mold limits the resolution of microstructures on soft shells for our demonstrations. More advanced fabrication technologies with higher resolution may offer an opportunity for more delicate structure generation. Based on the complex soft structures fabricated by flow casting, more abundant interactions, i.e., dynamic coloration, autonomous actuation, and feedback sensing ability, can be affiliated with the designs for soft robotics, wearable sensors, and other soft devices.

#### 4. Experimental Section

**Materials Preparation for Soft Shells:** Two different materials were used for all shell fabrication. The first one was Ecoflex 0050. Part A and part B of Ecoflex 0050 precursor were first stirred with equal volume for 1 min. Next, the precursor was vacuumed for 4 min to degas. Then, the material was prepared for the flow casting process. The other material was a mixture of Dragon skin 30 and Ecoflex 0030. Part A, part B of Dragon skin 30 precursors, and part A, part B of Ecoflex 0030 precursor were added into a beaker in sequence. The volume ratio of Dragon skin 30 and Ecoflex 0030 precursor was 2:1.

**Elastic Modulus and Demolding Tests for Soft Tubes:** The soft tubes with uniform layer thickness were prepared for elastic modulus measurement. Soft tubes were 2 cm long, 4 mm in outer diameter, and 500  $\mu\text{m}$  in thickness. Both ends of the soft tubes were clamped to the tensile testing machine (C42. 203, MTS) and then stretched with a 300  $\text{mm min}^{-1}$  strain rate at room temperature. Both Ecoflex 0050 and the mixture were tested three times (Figure S5, Supporting Information). For the demolding test, the soft tube's free length (5 mm) was left for clamping (see Figure 2E), and the total embedded length was 5 cm. After the sample was clamped to the tensile testing machine, a strain rate (300  $\text{mm min}^{-1}$ ) was applied to initiate the demolding process at room temperature.

**Surface Roughness Measurement:** A soft tube (outer diameter: 4 mm) with a uniform layer thickness was fabricated by a twice-casting process mentioned in the main text. Then, a 5 mm  $\times$  5 mm soft sheet was cut from the soft tube by a blade. This sample was prepared for inner and outer surface roughness tests by atomic force microscopy (Dimension Icon, Bruker). For the inner surface,  $S_a$  was 19.6 nm for a 25  $\mu\text{m}^2$  area, and  $S_a$  was 10.8 nm for a 1  $\mu\text{m}^2$  area. For the outer surface,  $S_a$  was 10.8 nm for a 25  $\mu\text{m}^2$  area, and  $S_a$  was 1.97 nm for a 1  $\mu\text{m}^2$  area (Figure S4, Supporting Information).

**Fabrication of Soft Shell of a Human-Hand Replica:** To replicate the delicate structure of human hands, plaster was chosen as the mold material, and the fabrication process was shown in Figure 3L. The plaster powder was first mixed with water to reach a paste state (mass ratio of powder:water = 5:3). Then, the hand of the subject was immersed into the paste. After the plaster was semisolidified, the hand was withdrawn from it. Next, the plaster was solidified at 60  $^\circ\text{C}$  for 12 h. Later, the elastic precursor (Ecoflex 0050) was poured into the rigid-hand mold and then turned over the mold to leak out the precursor. After the remaining layer was cured at room temperature overnight, the soft shell

was delaminated from the rigid mold. The white powders were observed on the soft replica (see Figure 3M,N) due to it falling off from the rigid mold.

**Fabrication of the Soft Vascular Replica:** The rigid vascular model was divided into segments and fabricated by a 3D printer (Formlab 3). The mixture was chosen to fabricate the soft replica. To generate a uniform layer, a second flow casting with the tube mold upside down was conducted. After all the precursors leaked out, the mold was fixed vertically and then placed at an elevated temperature (80  $^\circ\text{C}$ ) for quick curing. However, an inhomogeneous layer was inevitable due to the tortuous structure of the vascular model. The outer diameter of the soft replica was 4 mm, and 3D-printed rigid tubes (length: 5 mm, outer diameter: 4 mm, and layer thickness: 200  $\mu\text{m}$ ) were used to connect these soft segments in sequence. The red vascular replica was fabricated by mixing the elastomer precursor with the silicone color pigment (PMS 186C, Silc Pig, Smooth-On), as shown in Figure 4D. To coat a lubricant layer on the replica inner wall, the fabricated soft-shell segments were first soaked in benzophenone solution (10 wt% in ethyl alcohol) for 10 min, followed by air-drying. Then, the segments were soaked in the precursor of fluoropolymers (every 1 mL precursor consists of 800  $\mu\text{L}$  ethyl alcohol, 200  $\mu\text{L}$  1H,1H,2H-perfluoro-1-decene, and 2  $\mu\text{L}$  hydroxy-4'-(2-hydroxyethoxy)-2-methylpropiofenone) was cured under UV light for 1 h. Once cured, the excess solution was washed away by ethyl alcohol and air dried. Finally, lubricant oil Krytox 1506 (DuPont) was infused into the fluoropolymers to form a fluorogel, resulting in a lubricous gel-elastomer hybrid.

**Fabrication of the Small-Scale Soft Magnetic Robot:** The soft filament was first fabricated by dipping a needle into a thermoplastic resin melt (hot melt adhesive 3748Q, 3M) and then drawn out. After the filament was generated, a magnetic layer was attached by dipping the fiber into a composite precursor (Ecoflex 00–30 precursor, NdFeB, mass ratio = 1:2) and lifting it out. Finally, a uniform magnetic composite layer was coated on the soft filament after thermally curing, as shown in Figure 4D.

**Fabrication of Soft Sleeves for Rigid Grippers:** The adaptive gripper with a cubic geometry (length by width by height: 20 mm  $\times$  15 mm  $\times$  23 mm) was selected as the target. The rigid molds for flow casting were fabricated by a 3D printer (Formlab 3). In order to generate a fastening contact with the rigid gripper, the inner length was set as 18 mm, and the width was set as 13 mm. Later, a second flow casting was performed to generate a uniform thickness of the soft sleeves.

**Experiments of Friction Tests for Soft Sleeves:** For the friction test, the rigid gripper with soft sleeves was clamped at the bottom part of the tensile test machine (C42. 203, MTS). A 3D-printed cube (length by width by height: 22 mm  $\times$  20 mm  $\times$  25 mm) was connected to the top clamp of the machine by a string, and the gripper fixed the whole body of the cube with different loads (Figure S7, Supporting Information). All the tests were conducted at a 1  $\text{mm s}^{-1}$  stretch rate. All three structures (wedge-shaped, papillae, and foam) were applied to the shear tests. Figure S7 (Supporting Information) exhibited the friction–displacement curves under a 4 N load.

**Fabrication of Soft Optical Waveguides:** Ecoflex 0050 was chosen for the single soft optical waveguide. After a soft tube (inner diameter: 2 mm and length: 10 cm) with a uniform layer was prepared, the soft tube was filled with glycerol (99%, Energy Chemical). Then, both ends were capped by a blue RGB and a photodiode. Next, a small amount of the precursor was used for sealing the RGB and photodiode. After the precursor was cured, the waveguide was produced. To maintain the shape of the soft shell, the mixture was chosen for the three-branched optical waveguide fabrication. After the branched shell was fabricated, glycerol was injected. Then, three input branches were capped by red, green, and blue RGBs separately, and the top output branch was sealed by a small amount of the precursor. After the precursor was cured, the waveguide was prepared for later tests.

**Experiments of the Optical Waveguide:** The experimental test setup was built to obtain the change in the sensor's electrical signal output during stretching, as shown in Figure S8 (Supporting Information). Both ends of the sensor were fixed to the clamps of the tensile testing machine (C42. 203, MTS). The LED (Blue, brightness: 3000–

4000 mcd, GREELED) was powered with a 3.3 V power supply of the microcontroller unit (MCU) (Seeeduino XIAO, Seeed Inc.). The photodiode (SFH 229, Osram) was connected to the microcontroller unit via a photodiode amplifier. The photodiode amplifier (Figure S8, Supporting Information), which operated the photodiode in photovoltaic mode, was composed of an operational amplifier (OPAMP) (LM358, Texas Instruments Inc.), resistance ( $R_1 = 3 \text{ M}\Omega$ ) and capacity ( $C_1 = 6.7 \mu\text{F}$ ). During the stretching test, the sensor was stretched to 100% strain while the microcontroller unit sampled the voltage output  $V_{\text{out}}$  50 times per second and synchronously uploaded collected data to the computer via universal asynchronous receiver-transmitter (UART) communication. The stretching procedure was repeated three times.

The branched soft optical waveguide and color sensor (TCS34725 RGB Color Sensor, DFRobot) were fixed on the frame by a clamp, as shown in Figure S8 (Supporting Information). There were three different LEDs, a red one (wavelength 620–625 nm, GREELED), a blue one (wavelength 460–465 nm, GREELED), and a green one (wavelength 520–525 nm, GREELED), fixed into each branch of the soft shell, respectively. These LEDs were powered with a 5 V power supply of the microcontroller unit (Arduino UNO, Arduino). The color sensor was connected to a microcontroller unit via I2C communication. The output branch was faced with the photodiode array area of the color sensor. During the stretching test, each input branch was stretched to 50% strain in the direction of the axial of each branch, while the color sensor measured the output RGB intensity and sent it to the computer through the microcontroller unit. The stretching procedure was repeated three times.

**Statistical Analysis:** All data in this work were collected without preprocessing and presented as the mean  $\pm$  standard deviation. The sample size  $n$  for each experiment was at least 3 and had been indicated where applicable. Software used for data analysis included Origin and MATLAB.

## Supporting Information

Supporting Information is available from the Wiley Online Library or from the author.

## Acknowledgements

D.F., Y.L., and W.W. contributed equally to this work. This work was in part funded by the Science, Technology, and Innovation Commission of Shenzhen Municipality (grant No. ZDSYS20200811143601004, to H.W.), the National Natural Science Foundation of China (grant No. 52275021, to H.W.), the National Key R&D Program of China (grant No. 2022YFB4701200, to H.W.), the Natural Science Foundation of Liaoning Province of China (State Key Laboratory of Robotics joint funding, grant No. 2021-KF-22-11, to H.W.), the Southern Marine Science and Engineering Guangdong Laboratory (Guangzhou), (grant No. K19313901, to H.W.), the Stable Support Plan Program of Shenzhen Natural Science Fund Grant (No. K21326303, to C.Y.), and the Science, Technology, and Innovation Commission of Shenzhen Municipality (grant No. ZDSYS20210623092005017, to C.Y.). The authors acknowledge the assistance of SUSTech Core Research Facilities.

## Conflict of Interest

The authors declare no conflict of interest.

## Data Availability Statement

The data that support the findings of this study are available in the supplementary material of this article.

## Keywords

soft devices, soft shell fabrication, soft vascular replicas, soft waveguides

Received: September 29, 2022

Revised: November 27, 2022

Published online:

- [1] W. Xi, F. Kong, J. C. Yeo, L. Yu, S. Sonam, M. Dao, X. Gong, C. T. Lim, *Proc. Natl. Acad. Sci. USA* **2017**, *114*, 10590.
- [2] Y. Xia, G. M. Whitesides, *Annu. Rev. Mater. Sci.* **1998**, *28*, 153.
- [3] J. Shintake, V. Cacucciolo, D. Floreano, H. Shea, *Adv. Mater.* **2018**, *30*, 1707035.
- [4] D. Fan, X. Yuan, W. Wu, R. Zhu, X. Yang, Y. Liao, Y. Ma, C. Xiao, C. Chen, C. Liu, *Nat. Commun.* **2022**, *13*, 1.
- [5] T. J. Jones, E. Jambon-Puillet, J. Marthelot, P.-T. Brun, *Nature* **2021**, *599*, 229.
- [6] K. P. Becker, Y. Chen, R. J. Wood, *Adv. Funct. Mater.* **2020**, *30*, 1908919.
- [7] P.-G. De Gennes, *Rev. Mod. Phys.* **1992**, *64*, 645.
- [8] M. Rubinstein, R. H. Colby, *Polymer Physics*, Vol. 23, Oxford University Press, New York, **2003**.
- [9] E. Siéfert, E. Reyssat, J. Bico, B. Roman, *Nat. Mater.* **2019**, *18*, 24;
- [10] R. V. Martinez, J. L. Branch, C. R. Fish, L. Jin, R. F. Shepherd, R. M. Nunes, Z. Suo, G. M. Whitesides, *Adv. Mater.* **2013**, *25*, 205.
- [11] T. Gopesh, J. H. Wen, D. Santiago-Dieppa, B. Yan, J. S. Pannell, A. Khalessi, A. Norbash, J. Friend, *Sci. Rob.* **2021**, *6*, eabf0601.
- [12] H. Bai, S. Li, J. Barreiros, Y. Tu, C. R. Pollock, R. F. Shepherd, *Science* **2020**, *370*, 848.
- [13] P. A. Xu, A. K. Mishra, H. Bai, C. A. Aubin, L. Zullo, R. F. Shepherd, *Sci. Rob.* **2019**, *4*, eaaw6304.
- [14] R. L. Truby, M. Wehner, A. K. Grosskopf, D. M. Vogt, S. G. Uzel, R. J. Wood, J. A. Lewis, *Adv. Mater.* **2018**, *30*, 1706383;
- [15] K. Nan, S. Babae, W. W. Chan, J. L. Kuosmanen, V. R. Feig, Y. Luo, S. S. Srinivasan, C. M. Patterson, A. M. Jebran, G. Traverso, *Nat. Biomed. Eng.* **2022**, *6*, 1.
- [16] N. Kaneko, T. Mashiko, T. Ohnishi, M. Ohta, K. Namba, E. Watanabe, K. Kawai, *Sci. Rep.* **2016**, *6*, 1.
- [17] X. Li, X. Li, L. Li, Y. Meng, Y. Tian, *IEEE Robot. Autom. Lett.* **2021**, *6*, 8482;
- [18] Y. Wu, X. Dong, J.-k. Kim, C. Wang, M. Sitti, *Sci. Adv.* **2022**, *8*, eabn3431.
- [19] K. M. Digumarti, A. T. Conn, J. Rossiter, *J. R. Soc. Interface* **2018**, *15*, 20180301.
- [20] M. A. Bell, K. P. Becker, R. J. Wood, *Adv. Mater. Technol.* **2022**, *7*, 2100605.
- [21] J. Lim, A. R. Kim, S. Kim, S. Lee, D. Yoo, J. Park, J. Kim, *Adv. Mater. Interfaces* **2019**, *6*, 1901485.
- [22] J. N. Lee, C. Park, G. M. Whitesides, *Anal. Chem.* **2003**, *75*, 6544.
- [23] M. Schaffner, J. A. Faber, L. Pianegonda, P. A. Rühls, F. Coulter, A. R. Studart, *Nat. Commun.* **2018**, *9*, 878;
- [24] Y. F. Zhang, C. J. X. Ng, Z. Chen, W. Zhang, S. Panjwani, K. Kowsari, H. Y. Yang, Q. Ge, *Adv. Mater. Technol.* **2019**, *4*, 1900427.
- [25] A. Lee, P.-T. Brun, J. Marthelot, G. Balestra, F. Gallaire, P. M. Reis, *Nat. Commun.* **2016**, *7*, 11155.
- [26] N. P. Macdonald, J. M. Cabot, P. Smejkal, R. M. Guijt, B. Paull, M. C. Breadmore, *Anal. Chem.* **2017**, *89*, 3858.
- [27] J. A. Rogers, R. G. Nuzzo, *Mater. Today* **2005**, *8*, 50.
- [28] P. D. Marasco, J. S. Hebert, J. W. Sensinger, D. T. Beckler, Z. C. Thumser, A. W. Shehata, H. E. Williams, K. R. Wilson, *Sci. Rob.* **2021**, *6*, eabf3368.
- [29] J. M. Hahne, M. A. Schweisfurth, M. Koppe, D. Farina, *Sci. Rob.* **2018**, *3*, eat3630.

- [30] P. Puangmali, K. Althofer, L. D. Seneviratne, D. Murphy, P. Dasgupta, *IEEE Sens. J.* **2008**, *8*, 371.
- [31] T. Mashiko, K. Otani, R. Kawano, T. Konno, N. Kaneko, Y. Ito, E. Watanabe, *World Neurosurg.* **2015**, *83*, 351.
- [32] P. V. P. Reddy, V. Suresh, *Int. J. Mech. Eng. Robot. Res.* **2013**, *2*, 255.
- [33] Y. Lin, C. Zhang, W. Tang, Z. Jiao, J. Wang, W. Wang, Y. Zhong, P. Zhu, Y. Hu, H. Yang, *Adv. Sci.* **2021**, *8*, 2102539.
- [34] L. Picard, P. Phalip, E. Fleury, F. Ganachaud, *Prog. Org. Coat.* **2015**, *80*, 120.
- [35] K. Autumn, M. Sitti, Y. A. Liang, A. M. Peattie, W. R. Hansen, S. Sponberg, T. W. Kenny, R. Fearing, J. N. Israelachvili, R. J. Full, *Proc. Natl. Acad. Sci. USA* **2002**, *99*, 12252.
- [36] G.-B. Lee, C.-H. Lin, G.-L. Chang, *Sens. Actuators, A* **2003**, *103*, 165.
- [37] R. Abdurahman, A. Yimit, H. Ablat, M. Mahmut, J. De Wang, K. Itoh, *Anal. Chim. Acta* **2010**, *658*, 63.
- [38] T. Kim, S. Lee, T. Hong, G. Shin, T. Kim, Y.-L. Park, *Sci. Rob.* **2020**, *5*, eabc6878.
- [39] O. J. Schueller, X. M. Zhao, G. M. Whitesides, S. P. Smith, M. Prentiss, *Adv. Mater.* **1999**, *11*, 37.
- [40] A. Leber, C. Dong, R. Chandran, T. D. Gupta, N. Bartolomei, F. Sorin, *Nat. Electron.* **2020**, *3*, 316.
- [41] H. Zhao, K. O'Brien, S. Li, R. F. Shepherd, *Sci. Rob.* **2016**, *1*, eaai7529.
- [42] S. A. Morin, R. F. Shepherd, S. W. Kwok, A. A. Stokes, A. Nemiroski, G. M. Whitesides, *Science* **2012**, *337*, 828.
- [43] R. Lu, Q. Hong, Z. Ge, S.-T. Wu, *Opt. Express* **2006**, *14*, 6243.